doi: 10.82124/CEAS-GNC-2026-004

EuroGNC
Navigation
Guidance
Control
CEAS
Madrid, Spain
May 5th-7th
2026
uc3m Universidad Carlos III de Madrid
AIAA

Orbital Dynamics and Drag Area Estimation of PocketQubes with Passive Magnetic Attitude Control using TLE Data

Manuel Salema Project Manager & Systems Engineer @ Hydra Space Systems, 100506395@alumnos.uc3m.es, Madrid, Spain. manuel.salema.guilherme@gmail.com

ABSTRACT

PocketQubes are ultra-small satellites whose orbital lifetimes are strongly influenced by atmospheric drag and attitude dynamics, particularly when using passive magnetic attitude control (PMAC). Conventional prediction tools often assume fixed drag areas, overlooking the variability introduced by orientation and deployable structures.

This work develops a methodology that couples attitude propagation with SNAP, geometric area modelling, and GMAT-based orbit simulations, initialised from TLEs and enriched with space weather data. Results show that deployed configurations nearly double the effective drag area compared to folded states, significantly reducing orbital lifetime. Validation against historical TLEs indicates systematic biases of only 7 to 14 km, confirming the accuracy of the approach.

The proposed pipeline offers a reproducible framework for reliable lifetime prediction of passively stabilised PocketQubes, supporting mission planning, deorbit compliance, and constellation management.

Keywords: PocketQube, nanosatellite, passive magnetic attitude control, orbital dynamics, drag area estimation, orbital lifetime prediction, TLE data, GMAT, SNAP, space weather modelling, atmospheric drag, constellation management

Nomenclature

Ψ, Θ, Φ = Euler angles (yaw, pitch, roll) describing body orientation
$\mathbf{m}$ = Magnetic dipole moment vector (A·m^2)
$\mathbf{T}_{\text{mag}}$ = Magnetic torque, $\mathbf{T}_{\text{mag}} = \mathbf{m} \times \mathbf{B}$ (N·m)
$\mathbf{B}$ = Earth's magnetic field vector (T)
I_x, I_y, I_z = Principal moments of inertia about body axes (kg·m^2)
ω = Angular velocity vector in body frame (rad/s)
$A(\theta)$ = Instantaneous projected cross-sectional area (m^2)
$\bar{A}$ = Orbit-averaged effective drag area (m^2)
C_D = Drag coefficient (dimensionless)
β = Ballistic coefficient, $\beta = m/(C_D \bar{A})$ (kg/m^2)
m = Satellite mass (kg)
a_D = Acceleration due to atmospheric drag (m/s^2)

h = Altitude above mean Earth radius (km)
ρ = Atmospheric density (kg/m^3)
H = Scale height (km)
$F_{10.7}$ = Solar radio flux index (sfu)
Ap, Kp = Geomagnetic activity indices
SH = Empirical scale height from space-weather model (km)
DN = Density estimate from IPS/BoM model (kg/m^3)
a = Semi-major axis of orbit (km)
e = Eccentricity
i = Inclination (deg)
Ω = Right ascension of ascending node (deg)
ω = Argument of perigee (deg)
M = Mean anomaly (deg)
ν = True anomaly (deg)
μ_Δ = Mean altitude bias between theory and TLE (km)
σ_Δ = Dispersion of altitude residuals (km)

1 Introduction

PocketQubes (PQs) are ultra-small satellites (5 cm units) that enable low-cost missions for applications such as IoT connectivity and asset tracking [1, 2]. Their high area-to-mass ratio makes orbital lifetime highly sensitive to drag, while most PQs rely on Passive Magnetic Attitude Control (PMAC). This simple scheme aligns the satellite with Earth's magnetic field but couples attitude dynamics to aerodynamics: the projected cross-section, and thus drag, depends on orientation and deployment state. Assuming a constant reference area, as in many lifetime prediction tools, can therefore introduce systematic errors.

In practice, most lifetime-prediction tools for very small satellites assume fixed, idealised attitudes and a constant drag area. This is unrealistic for PocketQubes in low Earth orbit, whose orientation and effective cross-section evolve with magnetic alignment, residual spin, and deployment state. Because drag dominates the orbital decay process, even small errors in area modelling lead to significant lifetime bias. For operators, such inaccuracies affect mission planning, licensing, and constellation upkeep. The need for a lightweight, reproducible method linking PMAC-driven attitude behaviour to drag-area evolution and orbital decay was therefore the main motivation for this work.

1.1 Passive Magnetic Attitude Control and Detumbling

The adoption of PMAC is a heritage-proven solution for picosatellites when power and volume limits prevent active systems [3]. Research by Mesch [4] and Whisnant et al. [5] established the use of permanent magnets for alignment and hysteresis rods for energy dissipation. Recent research on the 3U AstroBio CubeSat [6] and the MRC-100 PocketQube [7] shows that, while PMAC provides reliable coarse stabilisation, performance is often limited by hysteresis saturation and residual oscillations [8]. These oscillations are most noticeable in high-area-to-mass platforms, where initial deployment-induced rates might take several orbits to damp [9], directly influencing the time-averaged drag area.

1.2 Orbital Decay and Drag Area Estimation

Traditional lifespan tools, like as ESA's DRAMA [10] and NASA's GMAT [11], frequently simplify picosatellites as spherical or fixed-attitude objects. However, for narrow geometries like PocketQubes, the coupling between attitude and orbit dynamics is considerable [12]. According to a recent study [13, 14], time-resolved attitude variations are necessary for separating density from drag: this distinction is critical for picosatellites, as atmospheric density fluctuations affect all surfaces equally, while the drag coefficient varies significantly as a function of the angle of attack relative to the satellite's specific geometry.

To enhance TLE-based decay predictions, this study directly links SNAP-propagated PMAC dynamics to a geometric area model, addressing the constraints of traditional models. Table 1 compares the proposed pipeline to the standard industry methods.

Table 1 Comparison of orbital lifetime prediction approaches for picosatellites.

Feature	**Standard Tools (DRAMA/GMAT)**	**Proposed Pipeline**
Attitude Model	Fixed / Idealized	Propagated (PMAC physics)
Drag Area	Constant Reference Area	Time-varying Geometric Area
Initial Conditions	Ideal Keplerian / Circular	TLE-derived State Vectors
Space Weather	Empirical Models with Preset or Averaged Solar Activity	Time-resolved, Mission-specific ($F_{10.7}$, Ap) Inputs
Coupling	Uncoupled	Integrated Attitude-Orbit

The proposed pipeline combines high-fidelity attitude propagation with SNAP [15], a geometric model of folded and deployed configurations, and GMAT-based orbit simulations initialized from TLEs. Atmospheric density is modelled as a function of altitude and contemporaneous space weather indices [16]. This integrated approach enables time-resolved drag estimation and provides a reproducible, validated framework for predicting the orbital lifetime of PMAC-stabilized PocketQubes.

2 Methodology

The analysis combines attitude propagation, geometry-based drag-area estimation, orbit propagation, and space-weather-aware density modelling in a single pipeline designed to predict orbital decay for PocketQube-class satellites with passive magnetic attitude control (PMAC). The methodology reflects the operational characteristics of a specific PocketQube bus, but it is intended to remain lightweight enough for constellation-scale use while retaining the essential physics that dominate lifetime in low Earth orbit (LEO).

2.1 Satellite Set and Initialisation

The study focuses on four PocketQube satellites — URESAT-1, HADES-D, HADES-R, and HYDRA-T — all based on the same 1.5P bus form factor, with a mass in the range of 0.38–0.40 kg and overall dimensions consistent with the PocketQube standard [1, 2]. The platforms can be flown in two distinct configurations: a *folded* (launch) configuration in which the deployable antennas remain wrapped around the body, and a *deployed* (mission) configuration in which the antennas are extended. Since the exposed aerodynamic cross-section and the inertia properties differ substantially between these two states, both are explicitly modelled.

Each satellite case is initialised from the first available post-launch Two-Line Element (TLE) set. The TLE provides the epoch, mean motion, inclination, right ascension of the ascending node (RAAN), eccentricity, argument of perigee, and mean anomaly, all expressed as SGP4 mean elements. These quantities are converted into classical orbital elements by numerically solving Kepler's equation to obtain the true anomaly from the mean anomaly, followed by computation of the semi-major axis from the mean motion. The resulting state is then mapped to an inertial Cartesian position and velocity vector. This process ensures that the propagated trajectory is dynamically consistent with the catalogue orbit at epoch rather than relying on an idealised reference orbit.

The same conversion procedure is applied to all four spacecraft, enabling a uniform comparison across the fleet and allowing differences in orbital evolution to be attributed to physical effects (e.g. drag area and deployment timing) rather than to inconsistent initialisation.

2.2 Attitude Propagation (SNAP)

The on-orbit attitude behaviour is propagated using the Smart Nanosatellite Attitude Propagator (SNAP) [15], a tool developed for nanosatellite-scale platforms operating under low-control or passively stabilised conditions. SNAP numerically integrates the rotational dynamics of the spacecraft under the action of environmental torques, including the geomagnetic torque, gravity-gradient torque, and aerodynamic torque. The Earth's magnetic field is modelled through the International Geomagnetic Reference Field (IGRF), which provides the local magnetic field vector $\mathbf{B}$ along the orbit.

The PocketQube bus under study relies on Passive Magnetic Attitude Control (PMAC). This stabilisation concept combines a permanent magnet, which produces a fixed magnetic dipole moment $\mathbf{m} \approx 0.71\,\mathrm{A} \cdot \mathrm{m}^2$ aligned with the chosen body axis, and two hysteresis rods made of high-permeability Permalloy-80, which act as passive magnetic dampers. The magnet tends to align the spacecraft with the Earth's magnetic field, generating a restoring torque $\mathbf{T}_{\mathrm{mag}} = \mathbf{m} \times \mathbf{B}$, while the hysteresis rods dissipate rotational energy through repeated magnetic domain realignment, thereby reducing rotational rates without active control authority. This approach provides coarse but power-free stabilisation and is standard for high area-to-mass ultra-small spacecraft.

To reflect the structural asymmetry introduced by the deployables, two inertia tensors are defined: one for the folded configuration and one for the deployed configuration. These inertia matrices, were derived from the CAD mechanical models of the bus and appendages, and capture the change in mass distribution introduced by the extended antennas. Since attitude dynamics in PMAC are sensitive to the inertia coupling terms, the use of configuration-specific inertia is necessary to reproduce the different oscillatory envelopes observed in flight.

All SNAP simulations are propagated for 100 h starting from an initial angular rate of 10°/s about the body axes. This initial rate is consistent with typical deployment-induced rotation at release from the deployer. The integration horizon of 100 h is sufficient for the transient spin to decay and for the PMAC system to approach its quasi-steady regime, which is characterised by bounded oscillation around a preferred alignment direction rather than strict static pointing. Aerodynamic torque is disabled in the present study because the default aerodynamic model within SNAP assumes CubeSat-like shapes and uniform mass distributions as well as no deployable structures, which are not representative of the slender, antenna-dominated geometry of the PocketQube platform under analysis.

A single SNAP configuration is used for all four satellites in the fleet. This choice is justified by the fact that the four PocketQubes share the same platform, PMAC hardware, and deployment architecture; mission-specific differences are dominated by (i) the timing of antenna deployment and (ii) the corresponding change in drag area. Consequently, attitude propagation results from the reference configuration can be carried through the rest of the pipeline as representative of the entire set.

Although a single SNAP configuration is used, manufacturing tolerances in magnetic moment magnitude and hysteresis rod properties may introduce dispersion in the damping behaviour and steady-state oscillation amplitudes. However, for the class of PocketQubes considered, these variations are expected to remain second-order effects compared to the dominant influence of deployment configuration on the effective drag area. As a result, the use of a representative configuration is considered sufficient for the purposes of orbit-averaged drag estimation.

Aerodynamic torque is disabled in the present SNAP study. This simplification is justified because, at the mission altitudes of 450–600 km, the magnetic restoring torque provided by the permanent magnet ($\sim 10^{-4}$ N·m) dominates the aerodynamic disturbance torque, which remains an order of magnitude lower for these slender geometries [17]. While coupled aero-magnetic effects are physically present, the magnetic dipole remains the primary driver of the quasi-steady oscillation envelope observed in flight.

Figure 1 illustrates, schematically, the expected PMAC behaviour: the long body axis tends to align with the local geomagnetic field while executing small oscillations along the orbit, resulting in a slowly precessing, weakly damped motion rather than a purely nadir-pointing state.

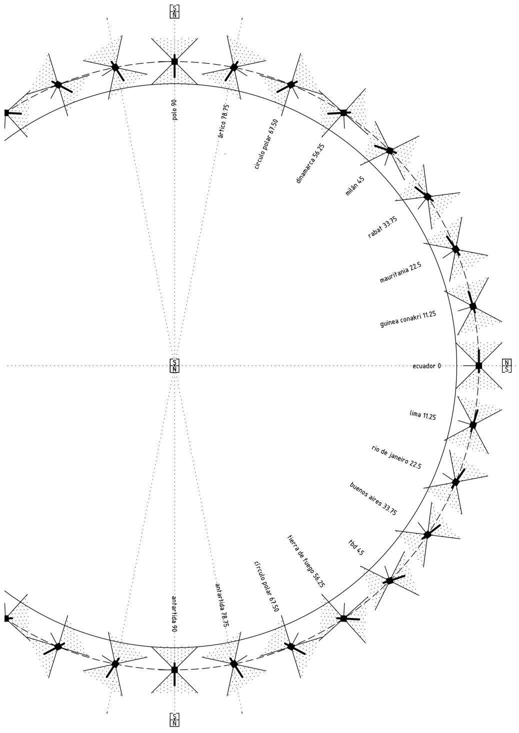

Fig. 1 PocketQube attitude alignment under PMAC along one orbit. The long axis aligns approximately with the geomagnetic field and exhibits small residual oscillations.

2.3 Geometry-Based Drag-Area Estimation

The aerodynamic interaction in LEO is strongly dependent on the instantaneous projected area normal to the velocity vector. For PocketQubes in particular, the contribution of thin, extended antennas can dominate the effective cross-section once deployed. A constant-area assumption, frequently used in traditional lifetime tools, is therefore not adequate for this class of spacecraft.

To resolve this, a composite geometric model of the spacecraft is constructed in Python. The model includes the main bus, the rail plate, and all deployable elements, with dimensions taken from the mechanical design definition of the Hydra Space PocketQube bus. Two discrete configurations are represented: the folded (launch) configuration and the deployed (mission) configuration. For each configuration, the full satellite geometry is described as a set of convex primitives whose vertices are known in the satellite body frame.

The body-frame geometry is then rotated according to the SNAP attitude output. SNAP provides the time history of Euler angles (yaw, pitch, roll) describing the spacecraft orientation in the local orbital frame over a representative orbit in the quasi-steady regime. For each sampled attitude state, the 3D mesh is rotated accordingly and orthogonally projected onto a plane normal to the instantaneous velocity direction. The resulting silhouette is converted into a 2D polygon, and overlapping polygonal regions are merged using geometric union operations (Shapely), preventing double-counting of internal occlusions.

This process yields:

1) the instantaneous projected area $A(\theta)$ as a function of orbital angle θ over one orbit, and
2) the orbit-averaged effective area $\bar{A}$ for that configuration.

The averaged area $\bar{A}$ is then used as the effective drag reference area in orbit propagation. This choice is motivated by two observations from the analysis: (i) the deployed configuration produces an orbit-mean area that is approximately twice that of the folded configuration, and (ii) the short-period fluctuations around $\bar{A}$, while physically meaningful, represent a small fraction of the mean and therefore have limited impact on long-term secular decay. The use of $\bar{A}$ thus captures the dominant effect (the configuration-dependent ballistic coefficient) while remaining computationally efficient.

2.4 Orbit Propagation (GMAT)

Orbital decay is simulated using the General Mission Analysis Tool (GMAT) [11], with the TLE-derived state at epoch serving as the initial condition and the configuration-dependent $\bar{A}$ from Section 2.3 used to define the ballistic properties of the spacecraft.

The force model includes the JGM3 gravity field (degree/order 4) and atmospheric drag. Solar radiation pressure (SRP) is disabled for this study, since at altitudes in the 450 km to 600 km regime the SRP-induced acceleration is significantly smaller than the drag acceleration and primarily contributes to long-term plane drift rather than to rapid decay in semi-major axis. This hierarchy of perturbations is consistent with standard LEO perturbation rankings, in which atmospheric drag dominates non-conservative effects below roughly 800 km.

Numerical propagation is performed using a Runge–Kutta 8(9) integrator with a relative error tolerance of 10^{-10} to ensure smooth, convergent altitude histories over the multi-month spans considered. The spacecraft dry mass is assigned according to platform specifications, while the drag coefficient is held constant at $C_D = 2.425$. While C_D is physically dependent on gas-surface interactions and atmospheric composition [18], a fixed value remains a standard and robust engineering approximation for this class of spacecraft [19]. In the LEO regime, the order-of-magnitude variations in thermospheric density ρ and effective cross-sectional area A are the dominant drivers of secular decay; therefore, the impact of C_D variability is treated as a secondary effect in this pipeline. Consequently, the drag model utilizes the orbit-averaged area $\bar{A}$ corresponding to the specific satellite configuration being analysed.

For URESAT-1, which is known to have transitioned from a folded to a deployed state after initial operations, the simulation switches from the folded $\bar{A}$ to the deployed $\bar{A}$ at the deployment date, thereby reflecting the step change in ballistic coefficient.

This GMAT configuration gives, for each satellite, a continuous theoretical altitude history $h_{\text{theory}}(t)$ that can be compared against the altitude inferred from the publicly available TLE set over the same time span.

2.5 Space Weather and Density Modelling

The neutral density of the thermosphere, and consequently the aerodynamic drag experienced by low Earth orbit satellites, is strongly modulated by solar and geomagnetic activity. To account for this variability, each TLE epoch is annotated with contemporaneous space weather parameters obtained from publicly available space environment records. The parameters considered include the 10.7 cm solar radio flux index ($F_{10.7}$), the centred 81-day average of $F_{10.7}$, the planetary geomagnetic index Ap, the Kp index, and the international sunspot number. These indices characterise the degree of solar EUV radiation and geomagnetic disturbance, both of which drive changes in thermospheric temperature and scale height, and are therefore widely used as inputs to empirical upper-atmosphere models.

The atmospheric density is approximated using the scale-height-based empirical model introduced in [16], which expresses the local density DN at altitude alt (in km) as

$$DN = 6 \times 10^{-10} \exp\left(-\frac{\mathrm{alt} - 175}{SH}\right) \quad \left[\mathrm{kg/m^3}\right], \tag{1}$$

where the effective scale height SH is determined as

$$SH = \frac{900 + 2.5\,(F_{10.7} - 70) + 1.5\,\mathrm{Ap}}{27 - 0.012\,(\mathrm{alt} - 200)} \quad [\mathrm{km}]\,. \tag{2}$$

In these expressions, the numerator of SH captures the combined effects of solar EUV heating (through $F_{10.7}$) and geomagnetic heating (through Ap), while the denominator provides an altitude-dependent adjustment related to the effective molecular mass variation within the upper atmosphere, valid within the 180 km to 500 km regime. The resulting DN reproduces the characteristic increase in thermospheric density during periods of enhanced solar or geomagnetic activity, and thus the corresponding amplification of atmospheric drag.

The drag acceleration applied in the orbit propagator follows the classical formulation:

$$\mathbf{a}_D = -\tfrac{1}{2}\, C_D\, \frac{A}{m}\, \rho\, V_{\mathrm{rel}}^2\, \hat{\mathbf{v}}_{\mathrm{rel}}, \tag{3}$$

where C_D is the drag coefficient, A the instantaneous or orbit-averaged projected cross-sectional area, m the spacecraft mass, ρ the atmospheric density from the empirical model, and V_{rel} the velocity of the spacecraft relative to the surrounding atmosphere. The direction $\hat{\mathbf{v}}_{\mathrm{rel}}$ is opposite to the instantaneous velocity vector. This expression, consistent with standard orbital drag formulations [20], underpins both the GMAT force model and the theoretical interpretation of TLE-derived orbital decay.

Within the simulation framework, the empirical density model and the drag law of Eq. (3) are employed in complementary roles. The density model provides a time-varying background consistent with observed solar and geomagnetic activity, while the drag formulation translates those conditions into an effective perturbing acceleration proportional to the spacecraft's area-to-mass ratio and the square of the relative velocity. Together, these elements ensure that the theoretical orbital decay accounts for both geometric and environmental variability, enabling a realistic comparison with the TLE-based orbital evolution.

2.6 Pipeline and Validation Strategy

The complete modelling chain can be summarised as follows:

1) Conversion of the first post-launch TLE for each satellite into classical orbital elements and inertial state at epoch.
2) Propagation of the spacecraft attitude using SNAP, including PMAC hardware (permanent magnet and hysteresis rods), realistic inertia tensors for folded and deployed configurations, and environmental torques.
3) Projection of the CAD-derived spacecraft geometry, rotated according to the SNAP attitude history, onto the plane normal to the velocity vector in order to obtain the instantaneous area $A(\theta)$ and the orbit-averaged effective drag area $\bar{A}$ for both folded and deployed states.

4) Orbit propagation in GMAT using the TLE-derived initial state, the configuration-dependent $\bar{A}$, a fixed drag coefficient C_D, and an atmospheric density model consistent with contemporaneous space weather.
5) Comparison of the propagated altitude history $h_{\text{theory}}(t)$ with the altitude inferred from the time-stamped TLE catalogue for the same spacecraft. The comparison is carried out interval-wise, where the theoretical altitude is averaged over each TLE validity interval and then differenced from the reported TLE altitude at the corresponding epoch. This yields the mean bias μ_Δ and dispersion σ_Δ used in Section 3 as validation metrics.

The resulting altitude biases must be viewed in the context of inherent TLE and atmospheric model limitations. Standard SGP4 propagation from TLE data is subject to position errors typically ranging from 1 to 5 km at epoch, which grow over time [21, 22]. Furthermore, empirical thermospheric density models can exhibit 15–20% uncertainty during periods of high solar activity [23]. Achieving a mean bias of 7–14 km over multi-month intervals demonstrates that the proposed pipeline effectively captures the dominant secular effects.

This structure allows direct assessment of how well a reduced-order but physically meaningful model — one that explicitly accounts for PMAC-driven attitude behaviour, configuration-dependent drag area, and space-weather-driven density — can reproduce observed orbital decay for ultra-small spacecraft. The methodology is therefore suitable both for post-flight reconstruction and for forward lifetime prediction.

3 Results and Analysis

3.1 SNAP Results

From the simulation configuration described in Section 2.2, SNAP [15] provides a comprehensive set of outputs describing the rotational dynamics and torque environment of the spacecraft, reflecting the coupling between its physical properties and the external perturbations modelled along the orbit. In this case, the software generates time histories of Euler angles, angular rates, environmental torque magnitudes, body- and orbit-referenced axes, as well as magnetic field alignments. This wealth of data makes it possible to assess not only the transient response of the passive magnetic system but also the long-term behaviour of the satellite as it approaches a damped steady state.

Among the different results available, one particularly illustrative output is the time evolution of the satellite's angular rotation rates, shown in Figure 2.

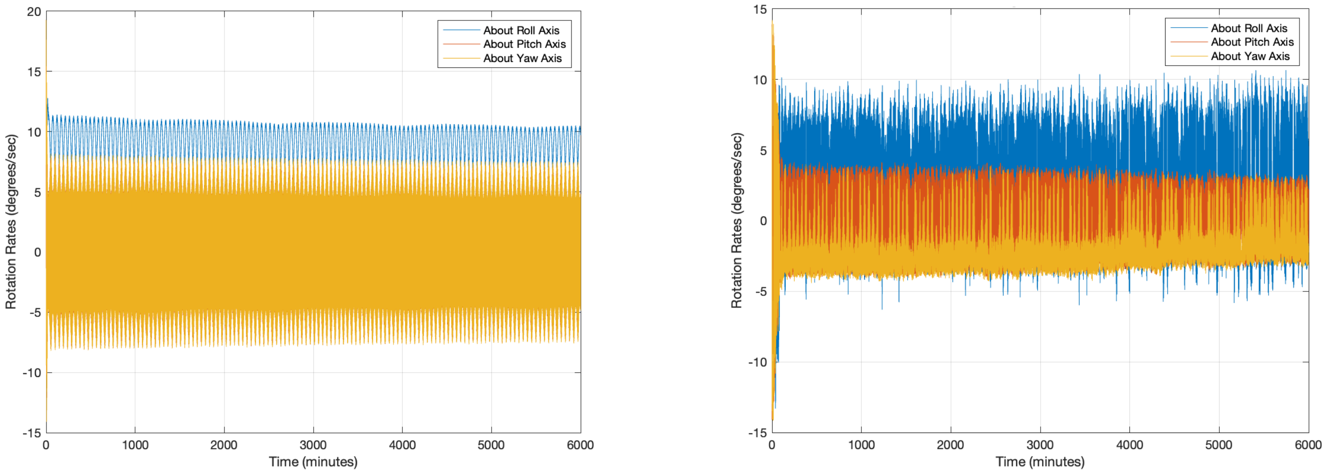

(a) Folded. **(b) Deployed.**

Fig. 2 Satellite angular rotation rates for different satellite configurations.

Figure 2 highlights how the initial rotational motion, imparted by launch and early orbit conditions, is progressively reduced by the combined effect of the permanent magnet and the hysteresis rods. However, the amplitude of the oscillations in the pitch and yaw axes remains significantly larger than anticipated. This behaviour supports the hypothesis that the hysteresis rods onboard Hydra Space PocketQubes are being partially saturated by the relatively strong permanent magnet - such saturation reduces the damping efficiency, preventing complete attenuation of the residual oscillations and leaving the spacecraft in a quasi-steady, oscillatory state. The magnet provides an aligning torque with respect to the geomagnetic field, while the hysteresis material dissipates rotational energy through magnetic domain realignment. This behaviour is corroborated by the environmental torque magnitudes shown in Figure 3, where the contributions of magnetic and damping torques dominate the overall evolution.

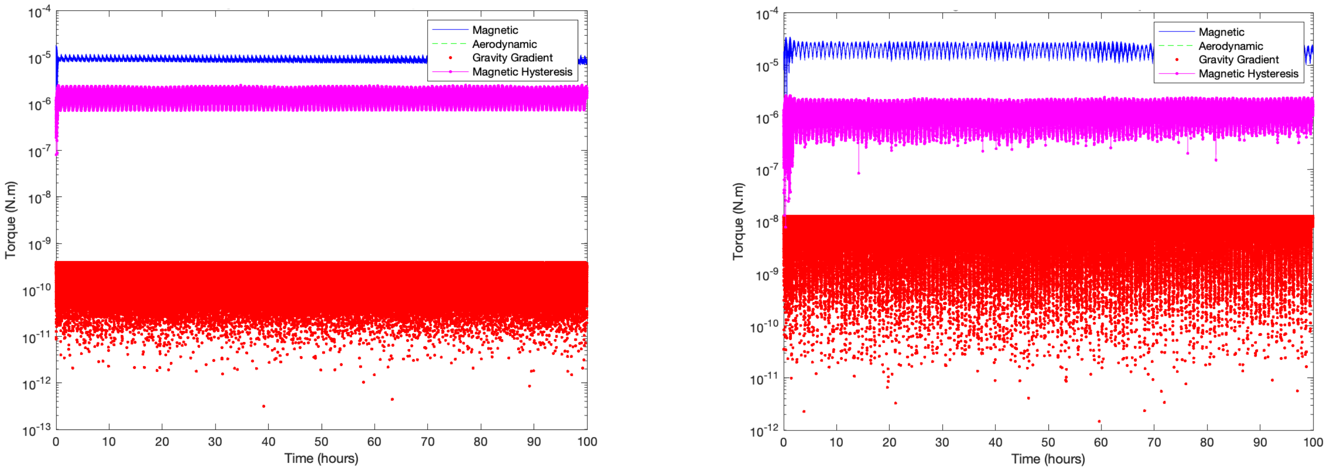

(a) Folded. **(b) Deployed.**

Fig. 3 Magnitude of environmental torques for different satellite configurations.

As a consequence, the angular velocity components decrease over time, eventually converging towards values near zero, consistent with a quasi-stable alignment regime.

Focusing now on this quasi-steady regime, and considering the final full orbit of the simulation, the most relevant outputs are the satellite main body axes relative to the nadir direction, presented in Figure 4.

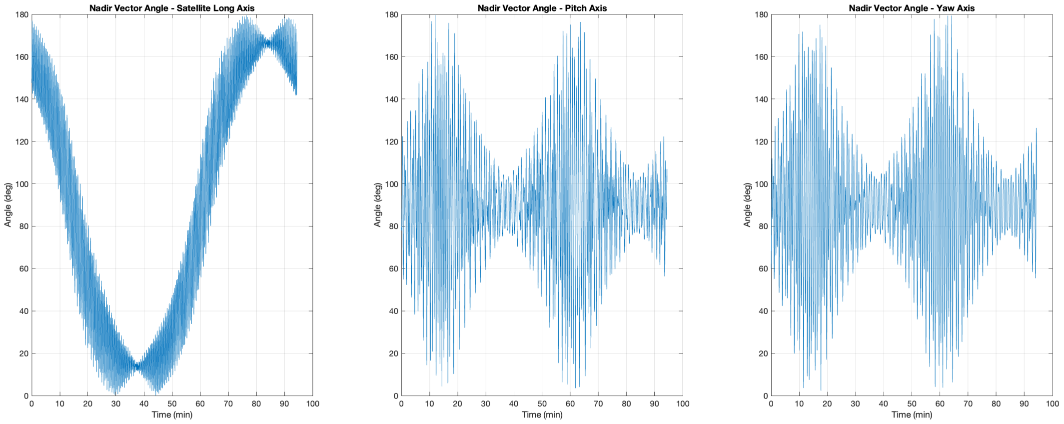

(a) Folded.

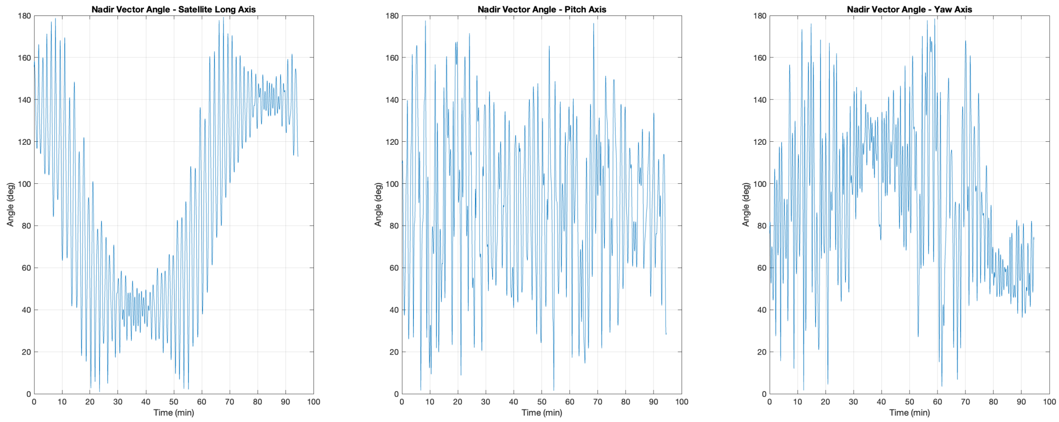

(b) Deployed.

Fig. 4 Satellite body axes relative to nadir vector over a full orbit. Each subfigure contains three panels showing, from left to right: nadir to roll axis, nadir to pitch axis, and nadir to yaw axis.

From a theoretical standpoint, the roll axis—corresponding to the satellite's long axis—should exhibit the characteristic alignment behaviour discussed in Section 2.2 (see Figure 1). Although that schematic neglects the displacement of the Earth's magnetic dipole, it nevertheless captures the essential feature: the long axis oscillates around a preferred equilibrium direction as the spacecraft aligns magnetically along the orbit.

Focusing on the long-axis evolution in Figures 4a and 4b, the simulation results are consistent with the expected behaviour. The apparent variations arise from a residual oscillation of the axis around its equilibrium orientation, interpretable as a gyroscopic precession effect. In practice, the satellite behaves like a spinning top, with the long axis tracing a small oscillatory motion rather than remaining fixed. The difference in oscillation amplitude between the two configurations is explained by distinct inertia properties: in the deployed case, mass distribution shifts towards the central body, while the antenna asymmetry generates imbalance. This imbalance, stemming from the inertia matrix and amplified by differential drag on the antennas, is also evident in the pitch and yaw axes, leading to the more pronounced oscillations observed after deployment.

3.2 Area Estimation Results

The first step, is to confirm the correct modelling of the satellite.

(a) Folded Antennas

(b) Deployed Antennas

Fig. 5 Modelled Satellite Configurations

Figure 5 confirms and validates the correct modelling of the satellite with respect to Hydra Space PQ platform specifications. This allows to proceed with the next step, which goal is to model the satellite along the orbit, computing the satellite wet area, also known as, the satellite cross-sectional area, which is the area of the satellite that is exposed to orbital perturbations, by implementing the SNAP output file of the satellite main axes relative to the nadir vector, for both configurations, and rotating the satellite at each know point over a full orbit.

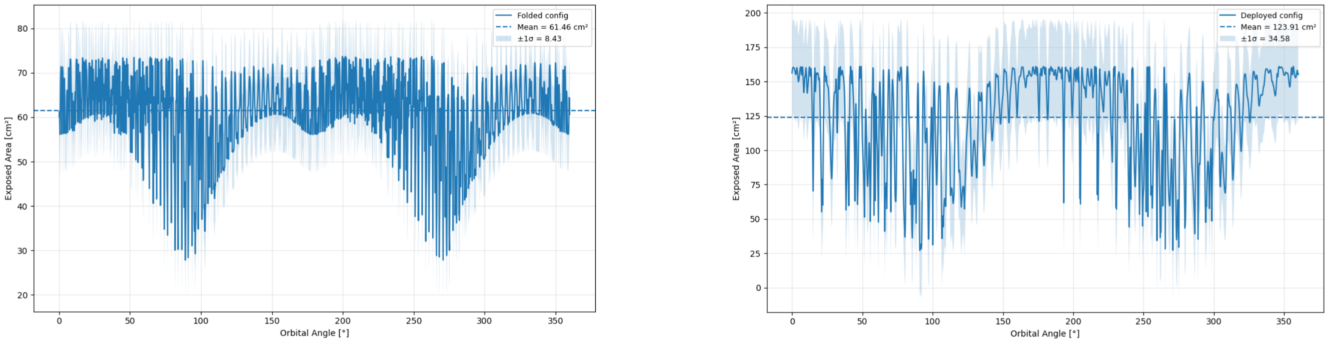

(a) Folded Configuration **(b) Deployed Configuration**

Fig. 6 Estimated Wet Area of the Satellite over Orbital Angle

Figure 6 provides an visual analysis of how the satellite cross-sectional area changes over an orbit. Ideally, the oscillation that exists near a certain orbit angle, should be almost minimal, but as explained in 3.1 since the hysteresis rods are saturated by the magnet, they don't effectively damp the oscillations around the pitch and yaw axes, and consequently, affecting the cross-sectional area over an orbit.

Table 2 Satellite Cross-Sectional Area according to their configurations.

Configuration	**Avg. Area (m^2)**
Folded Antennas	0.0062
Deployed Antennas	0.0124

Table 2 summarises the results for the average cross-sectional area of Hydra Space PocketQubes for both folded and deployed configuration, this results are crucial for the Dry Area input used in the GMAT simulation 2.3.

3.3 GMAT Results

Using the orbital propagation setup described in Section 2.3, each satellite was simulated in GMAT from launch until atmospheric re-entry. The objective of these runs was to quantify the altitude evolution over the mission lifetime under a consistent dynamical environment and with the effective drag area fixed to the values obtained in the previous analysis. The resulting altitude profiles for the four satellites under study—HADES-D, HADES-R, HYDRA-T, and URESAT-1—are presented in Figure 7. These plots illustrate the progressive orbital decay driven primarily by atmospheric drag, with each case reflecting the influence of its specific mass and cross-sectional area on the rate of altitude loss.

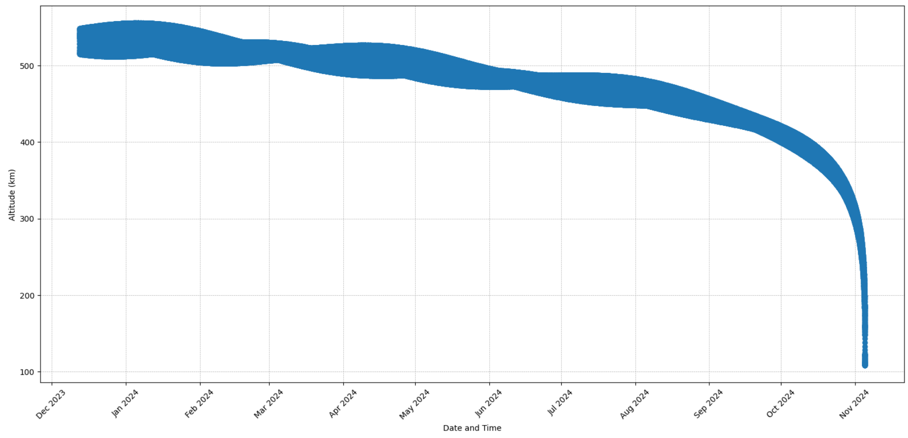

(a) HADES-D

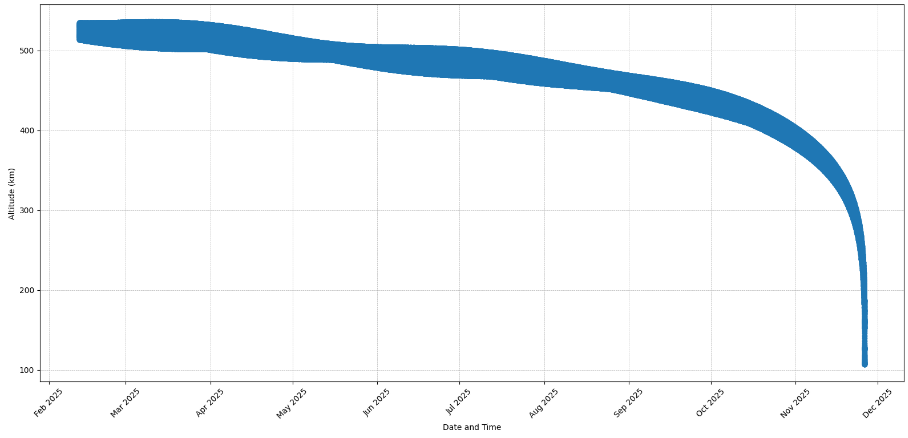

(b) HADES-R

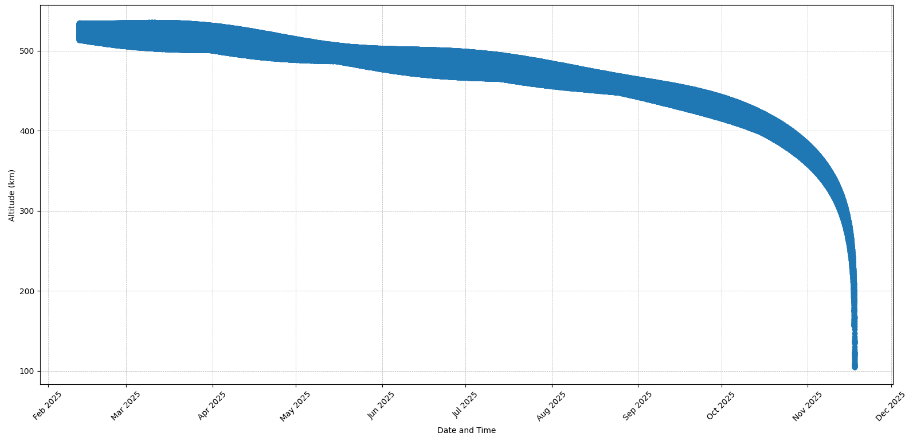

(c) HYDRA-T

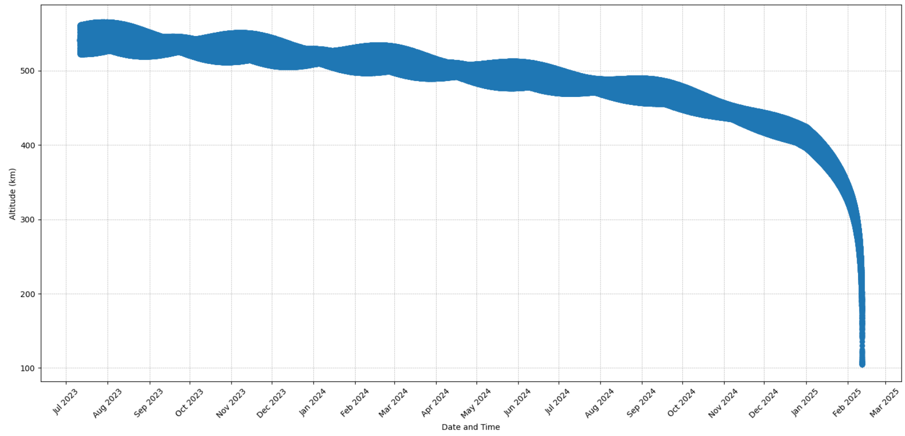

(d) URESAT-1

Fig. 7 GMAT:Orbit Simulation

3.4 TLE Results

This section presents the results derived from the processing of historical TLE datasets for the Hydra Space PocketQube satellites. For each spacecraft, all publicly available TLEs were collected and parsed into structured datasets covering the full operational lifetime, from launch until decay (when applicable). These datasets formed the basis for extracting orbital and environmental parameters, as well as for deriving secondary quantities such as drag force and deceleration.

The processing chain follows a systematic sequence: first, the TLEs are converted into classical orbital elements, Cartesian state vectors, and LLA coordinates. Next, environmental conditions are synchronised to the TLE epochs, incorporating solar flux and geomagnetic activity indices as described in Section 2.5. Using the atmospheric density model introduced in Section 2.5, the instantaneous density was then computed for each epoch. Finally, with the satellite areas assigned according to Section 3.2 and the drag model described in Equation 3, the drag force and corresponding deceleration were obtained consistently across the dataset.

The results are presented in three main parts. First, the orbital evolution is analysed in terms of the Keplerian elements extracted from the TLEs. Second, the space weather conditions relevant to atmospheric density variations are reviewed and linked to the observed orbital behaviour. Finally, the evolution of drag force is quantified for each satellite, illustrating the combined effects of geometry, mass, and environmental variability.

3.4.1 Keplerian Elements

After parsing all TLE historical data, which is a txt file that contains all observed TLE data of a specific satellite for a certain epoch, into a data structure for each satellite, the first step is to analyse and compare the keplerian elements of the satellite with the ones shown in CelesTrak, a website responsible for providing TLE data for all satellites in orbit.

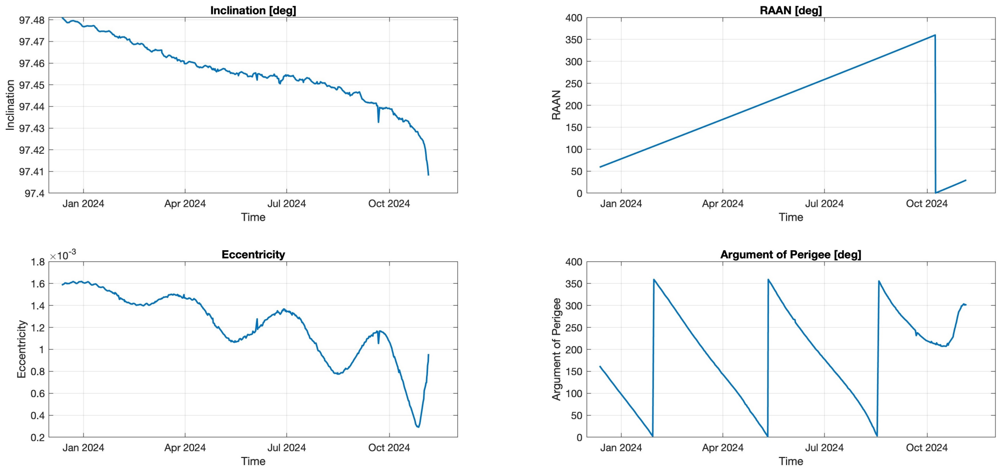

(a) HADES-D

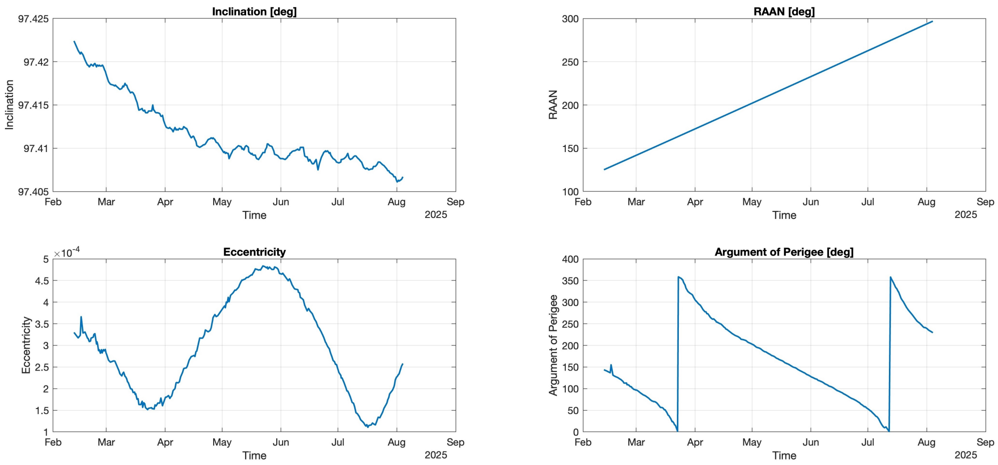

(b) HADES-R

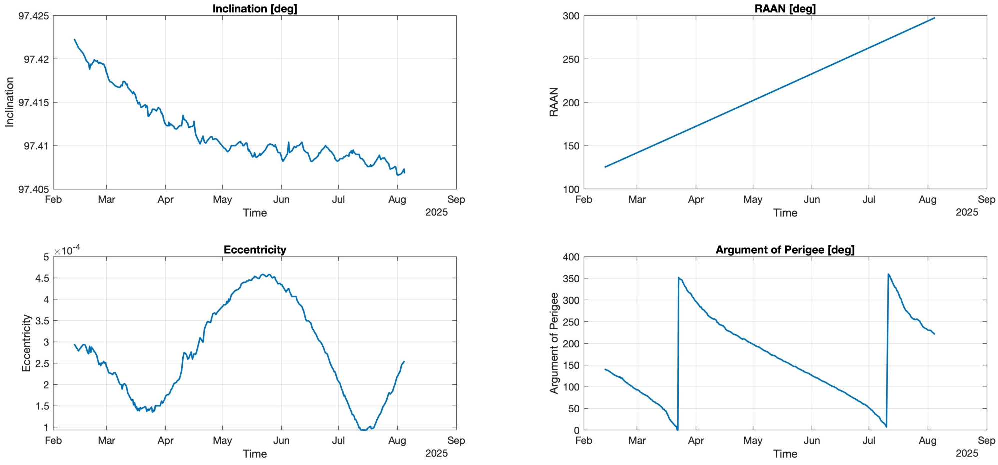

(c) HYDRA-T

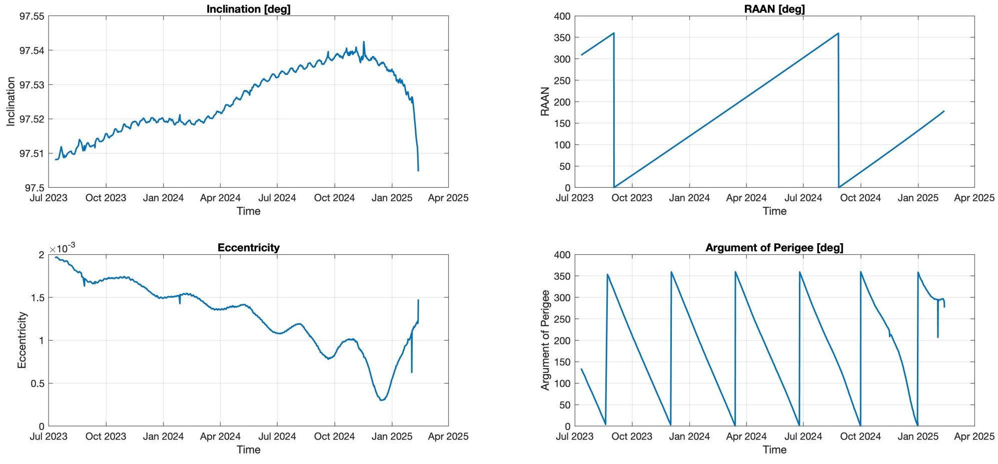

(d) URESAT-1

Fig. 8 Keplerian elements evolution for the analysed satellites. Each subfigure contains four panels showing, from left to right and top to bottom: inclination, right ascension of the ascending node (RAAN), eccentricity, and argument of perigee.

This results shown in Figure 8 are a direct interpretation of historical TLE data from each satellite, they have then been validated with plots shown in websites such as CelesTrak, SatNOGS and Space-Track.

Altitude

Focusing on the altitude of each Hydra Space PQ over time, two plots can be seen in Figure 9, one represents the each satellite altitude over time from launch to their last known TLE data or until decay if that is the case.

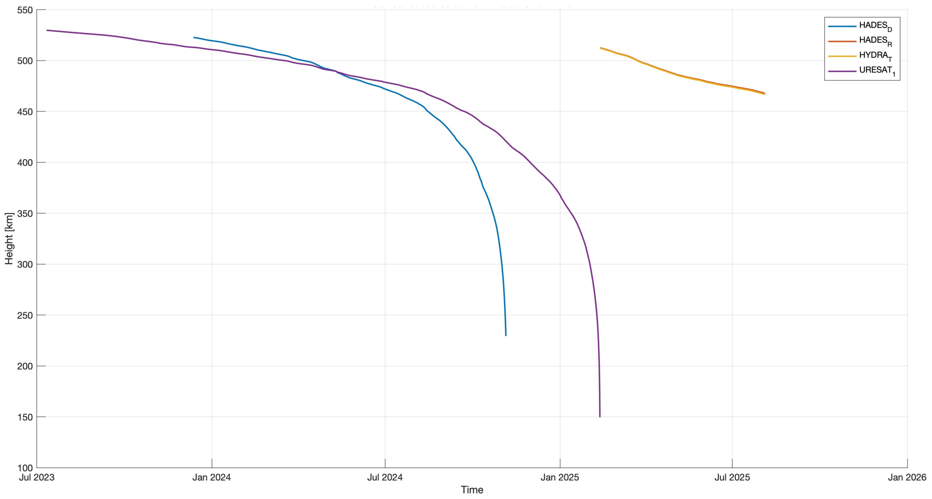

(a) Satellite Altitude over Time

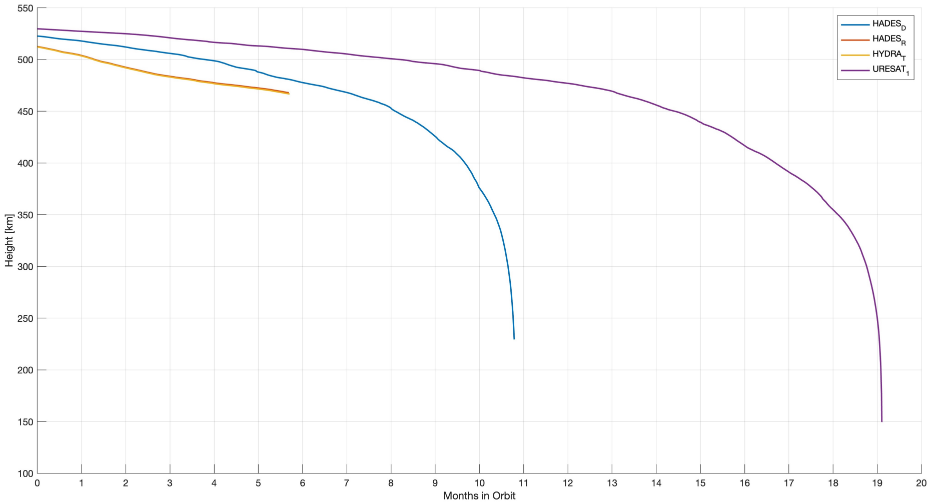

(b)

Fig. 9 Satellite Altitude over Normalised Time

From Figure 9a it is clear that even though HADES-D was launched almost 5 months after URESAT-1 (11th of November 2023 and 12th of June 2023, respectively) URESAT lasted around 9 months more time in orbit then HADES-D, this can be explained due to the known malfunction of the antennas on URESAT-1 after deployment, which have then been later found out that only during January 2025 the antennas finally deployed. Regarding HADES-R and HYDRA-T both satellites were launched in Q1'25, aboard of the same launcher and in the same satellite deployer (launched on the 14th of January 2025), and both of them show the same behaviour, which is expected, since they share the same SSO orbit, same PQ format and platform, and only differ in a total of 11 grams.

3.4.2 *Space Weather*

With the help of the script described in 3.4.2, focusing on the most relevant parameters from the dataset a detailed time-synchronized representation of space weather conditions, enabling the analysis of environmental effects on satellite dynamics and operations.

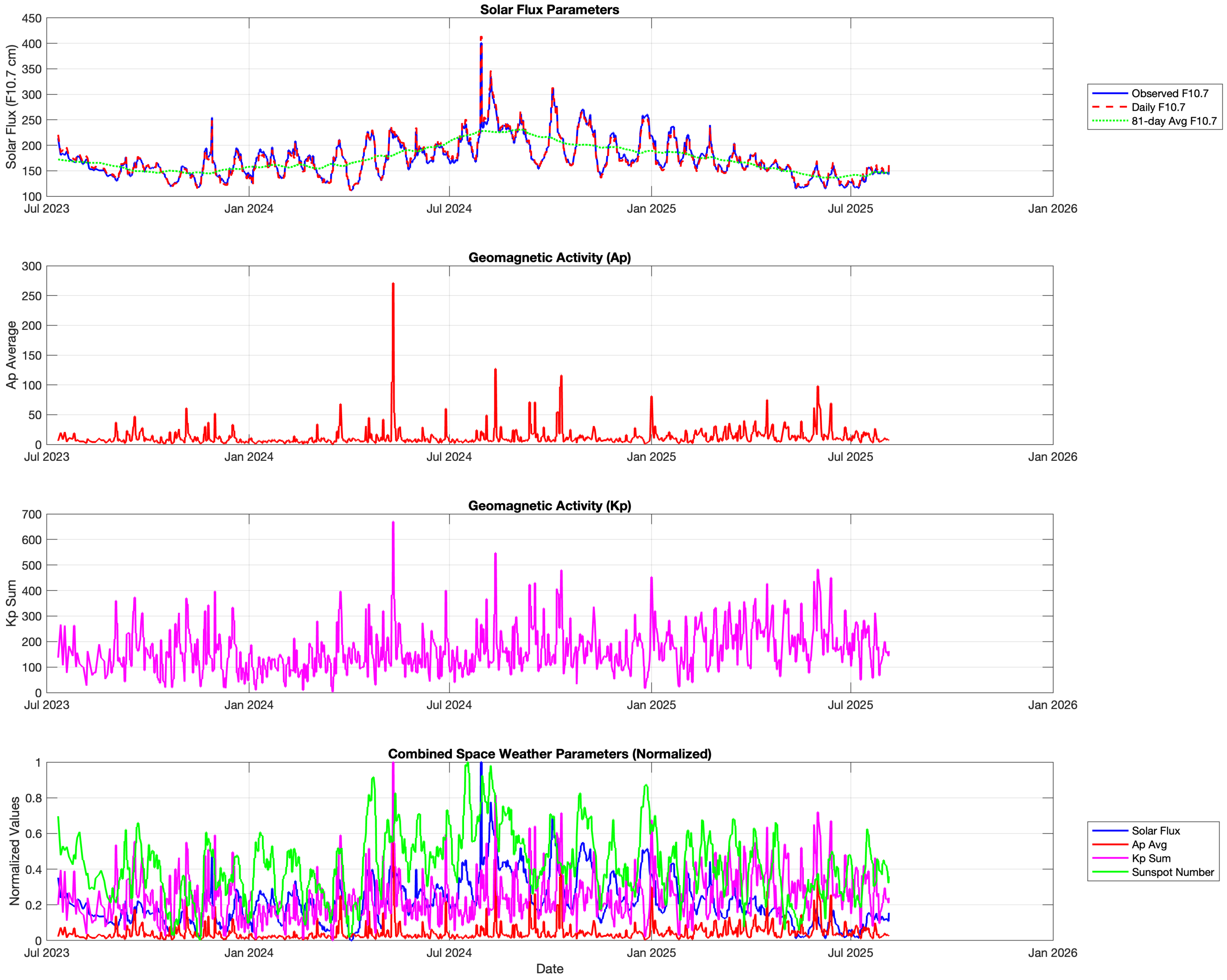

Fig. 10 Space Weather

Figure 10 different space weather aspects can be seen, such as the solar flux parameters, the Ap index, Kp index, and a combined of the most relevant space weather parameters at the bottom. The solar flux parameters, in specific the F10.7, is a key indicator of solar activity and is used to estimate the thermospheric density, which in turn affects the drag force experienced by satellites in orbit. The Ap index is a measure of geomagnetic activity, which can influence the density of the upper atmosphere and the satellite's orbital dynamics. The Kp index is another geomagnetic activity indicator, providing insights into the potential impact of magnetic disturbances on satellite operations. Lastly, the combined space weather parameter provides a comprehensive overview of the solar and geomagnetic conditions that may have influenced the satellite's orbit over time.

3.4.3 Drag

With the area estimation results from 3.2 and the atmospheric density model, as seen in 2.5, the drag force can be dynamically computed for each TLE epoch within each satellite according to the formulation in Eq. (3).

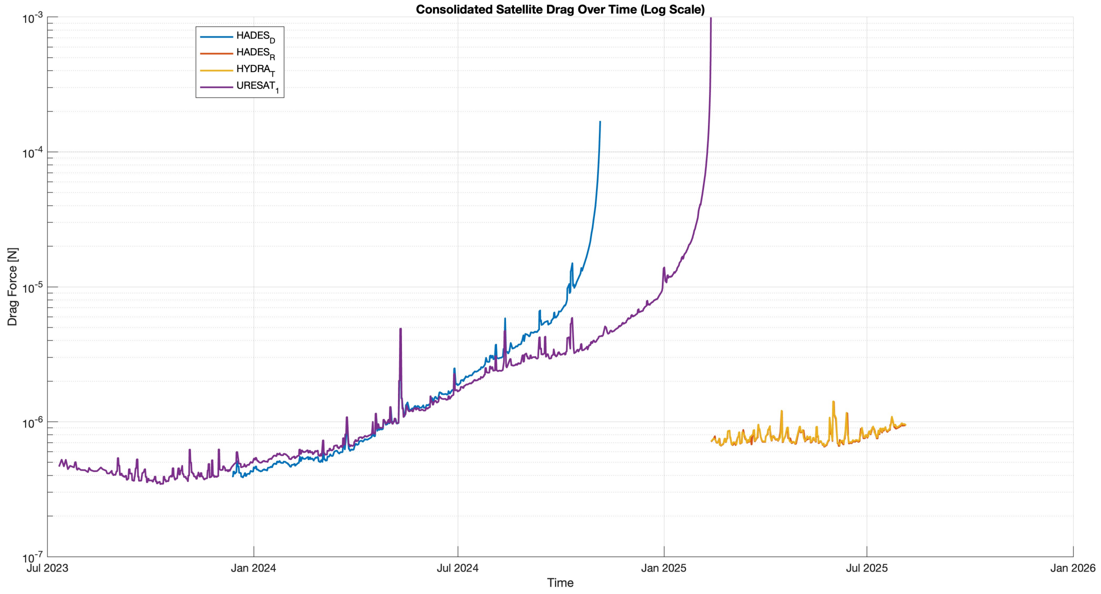

Fig. 11 Satellite Drag

Figure 11 shows the evolution of drag force for the four PocketQubes considered. The results highlight clear differences in orbital behaviour: URESAT-1 and HADES-D exhibit steadily increasing drag as their altitudes decay, with a sharp rise during the final months before re-entry. By contrast, HADES-R and HYDRA-T, both inserted into slightly lower orbits, show nearly constant drag levels during the available observation window. This behaviour reflects both their shorter time in orbit and the solar flux conditions present at the time of launch (see Figure 10), which amplified atmospheric density variations despite their similar altitudes.

The order-of-magnitude fluctuations observed for URESAT-1 and HADES-D correlate strongly with density enhancements driven by solar and geomagnetic activity, confirming the dominant role of space weather in drag variability.

Overall, this analysis demonstrates that the combination of realistic area modelling and dynamic atmospheric inputs captures not only the long-term drag-driven decay trend but also short-term variability. These results validate the importance of time-resolved drag estimation when predicting the orbital lifetime of passively stabilized nanosatellites.

3.5 Theoretical Vs Empirical: Comparison and Validation

The complete modelling pipeline developed in this work combines three stages: (i) attitude dynamics from SNAP, capturing the realistic orientation of the satellite under passive magnetic control; (ii) Python-based geometric modelling, which uses the SNAP outputs to estimate the instantaneous and orbit-averaged drag area; and (iii) orbital propagation in GMAT, where the estimated area is introduced into the force model together with the environmental perturbations described in Section 3.3. This sequence produces a theoretical prediction of orbital decay that incorporates both the spacecraft's physical properties and its environment.

To validate the fidelity of this approach, the theoretical altitude histories were compared with the empirical record given by the TLE catalogue. Since TLEs describe mean orbital states at discrete epochs rather than instantaneous quantities, the comparison was performed on a like-for-like basis by computing, for each TLE epoch t_i, the *interval-averaged* theoretical altitude $\langle h_{\text{theory}} \rangle_i$ over the TLE's domain of validity.

Letting $\{t_i\}_{i=1}^{n}$ be the sequence of TLE epochs (sorted), and τ_i the midpoints between consecutive epochs, the interval $\mathcal{I}_i$ associated with t_i is defined as:

$$\mathcal{I}_i = \begin{cases} \left[t_1,\, \tau_1\right], & i = 1, \\ \left[\tau_{i-1},\, \tau_i\right], & 1 < i < n, \\ \left[\tau_{n-1},\, t_n\right], & i = n, \end{cases} \tag{4}$$

The theoretical altitude is then averaged over this interval:

$$\langle h_{\text{theory}} \rangle_i = \frac{1}{|\mathcal{I}_i|} \int_{\mathcal{I}_i} h_{\text{theory}}(t)\, \mathrm{d}t \tag{5}$$

and the difference with respect to the TLE altitude is:

$$\Delta_i = \langle h_{\text{theory}} \rangle_i \; - \; h_{\text{TLE}}(t_i) \tag{6}$$

The global bias μ_Δ and dispersion σ_Δ are obtained as the mean and standard deviation of Δ_i across all epochs with coverage overlap. A positive μ_Δ indicates that the theoretical model predicts higher altitudes (i.e. slower decay) than observed by TLEs.

Table 3 summarises the results, observed in Figure 12, for the four satellites, where the theoretical model corresponds to the full SNAP–Python–GMAT pipeline.

Table 3 Comparison between theoretical predictions and empirical TLE evolution.

Satellite	μ_Δ (km)	σ_Δ [(km)
HADES-D	+7.327	4.313
HADES-R	+11.617	3.909
HYDRA-T	+10.746	4.482
URESAT-1	+14.067	10.057

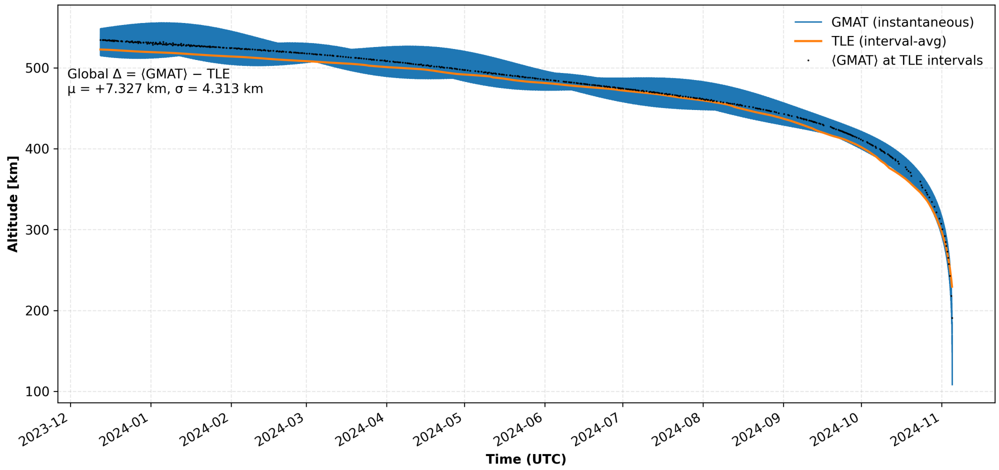

(a) HADES-D

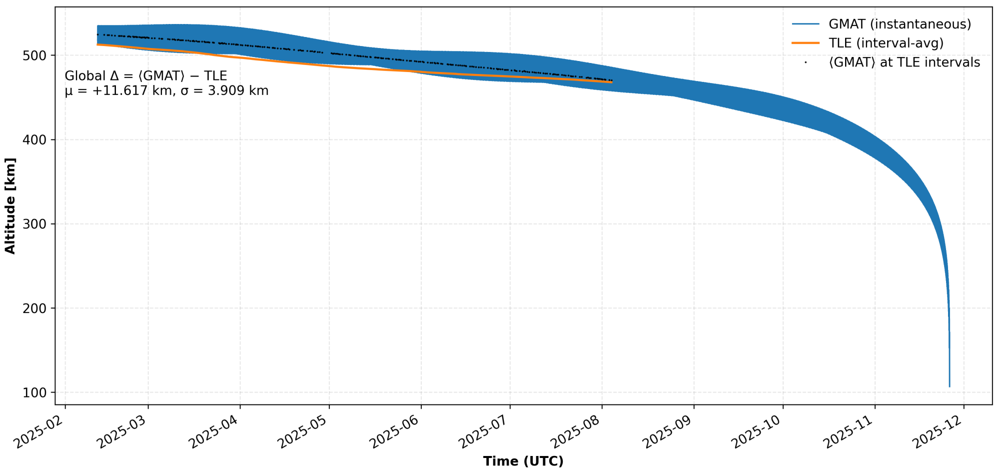

(b) HADES-R

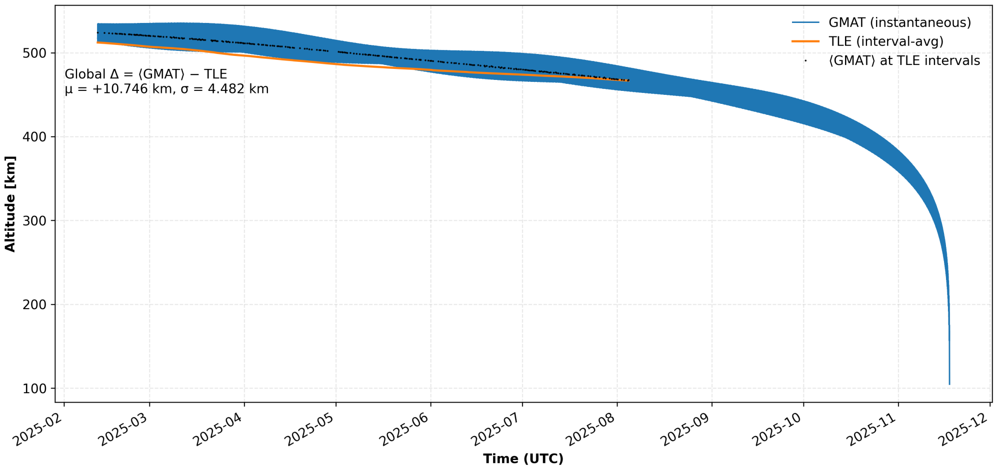

(c) HYDRA-T

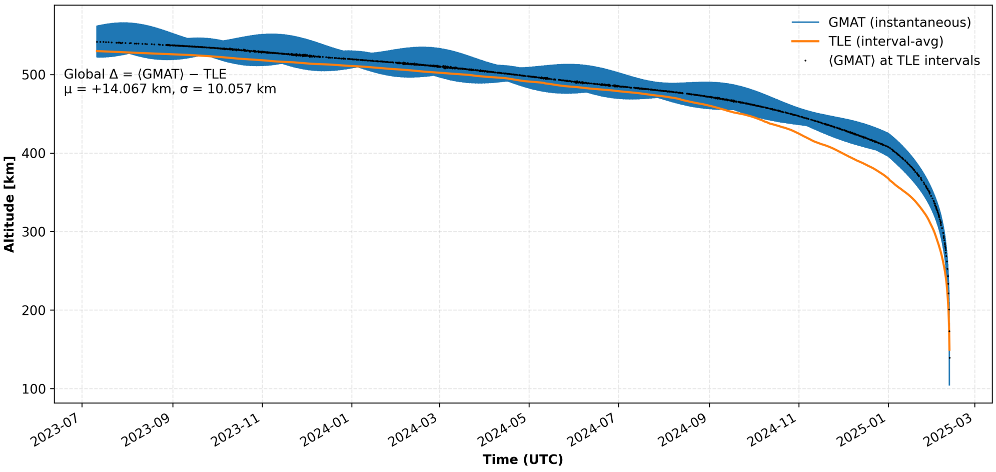

(d) URESAT-1

Fig. 12 GMAT Vs TLE orbit comparison

Figure 12 demonstrates a strong agreement between the theoretical predictions of the SNAP–Python–GMAT pipeline and the empirical orbital evolution derived from TLEs. Across all satellites, the model reproduced the observed decay trends with mean biases (μ_Δ) of only 7–12 km for HADES and HYDRA, and $\sim$ 14 km for URESAT-1. Given that these results stem from months of propagation, and considering the intrinsic uncertainties in TLE accuracy and atmospheric density modelling, such levels of agreement confirm the robustness of the methodology.

The slightly higher bias and dispersion (σ_Δ) observed for URESAT-1 are consistent with its late antenna deployment and the resulting change in drag area, which introduced additional variability not present in the other cases. For all remaining satellites, the dispersion remains below 5 km, underscoring the fidelity of the model in reproducing both long-term decay trends and short-term fluctuations.

Overall, these results validate the developed approach: by coupling attitude dynamics, realistic area modelling, and orbit propagation with environmental variability, the methodology achieves predictive accuracy that is fully consistent with empirical records and well within the limits of current orbital analysis for small satellites.

4 Conclusion

This work developed and validated a modelling pipeline for PocketQube satellites with passive magnetic attitude control, explicitly linking attitude dynamics to aerodynamic drag and orbit decay. By coupling SNAP-based attitude propagation, geometry-driven drag-area estimation, GMAT orbit propagation, and space-weather–responsive density modelling, the approach captures configuration-dependent variability in projected area and its impact on orbital lifetime.

Results show that deployed configurations nearly double the effective drag area compared to folded states, leading to significantly faster decay. SNAP simulations revealed quasi-stable but oscillatory magnetic alignment, which propagates into drag-area fluctuations. Validation against historical TLEs demonstrated strong agreement, with mean altitude biases of 7–12 km for HADES and HYDRA and ~14 km for URESAT-1, consistent with its delayed antenna deployment. These levels of accuracy confirm the robustness of the pipeline for predicting the orbital lifetime of PMAC nanosatellites.

The methodology provides a reproducible framework for reliable decay prediction, supporting mission planning, deorbit compliance, and constellation management. Future extensions will target refined drag modelling (geometry, surface properties, lift) and further analysis of residual magnetic torques on long-term stability.

Acknowledgments

This work is an extended and updated consolidation of the research originally conducted as the Master's Thesis at Universidad Carlos III de Madrid (UC3M), with additional post-flight analysis and validation against on-orbit data.

Declaration of Use of Artificial Intelligence

Artificial intelligence was not used in the work presented.

References

[1] Silvana Radu, M. S. Uludag, S. Speretta, Jasper Bouwmeester, A. Menicucci, A. Cervone, Andrew Dunn, Tom Walkinshaw, Pedro Luiz Kaled Da Cas, Chantal Cappelletti, and Filippo Graziani. *The PocketQube Standard, Issue 1.* TU Delft, Alba Orbital, GAUSS Srl, June 2018. Available online: `https://static1.squarespace.com/static/53d7dcdce4b07a1cdbbc08a4/t/5b34c395352f5303fcec6f45/1530184648111/PocketQube+Standard+issue+1+-+Published.pdf`.

[2] NASA Small Spacecraft Systems Virtual Institute. State-of-the-art small spacecraft technology: Chapter 2 – spacecraft platforms. Technical Report NASA/TP–20210023410, National Aeronautics and Space Administration (NASA), 2023. `https://www.nasa.gov/smallsat-institute/sst-soa/platforms/`.

[3] Halis Polat, Josep Virgili-Llop, and Marcello Romano. Survey, statistical analysis and classification of launched cubesat missions with emphasis on the attitude control method. *Journal of Small Satellites*, 5:513–530, 01 2016.

[4] F. Mesch. Magnetic components for the attitude control of space vehicles. *IEEE Transactions on Magnetics*, 5(3):586–592, 1969. doi: 10.1109/TMAG.1969.1066581.

[5] J. M. WHISNANT, D. K. ANAND, V. L. PISACANE, and M. STURMANIS. Dynamic modeling of magnetic hysteresis. *Journal of Spacecraft and Rockets*, 7(6):697–701, 1970. doi: 10.2514/3.30022.

[6] Stefano Carletta, Augusto Nascetti, Sagar S. Gosikere Matadha, Lorenzo Iannascoli, Thiago Baratto de Albuquerque, Nithin Maipan Davis, Luigi Schirone, Gabriele Impresario, Simone Pirrotta, and John R. Brucato. Characterization and testing of the passive magnetic attitude control system for the 3u astrobio cubesat. *Aerospace*, 9(11), 2022. ISSN: 2226-4310. doi: 10.3390/aerospace9110723.

[7] Tibor Herman and Levente Dudás. The redundant attitude control system of mrc-100 pocketqube satellite. In *2023 New Trends in Aviation Development (NTAD)*, pages 95–99, 2023.

[8] Assal Farrahi and Ángel Sanz-Andrés. Efficiency of hysteresis rods in small spacecraft attitude stabilization. *The Scientific World Journal*, 2013(1):459573, 2013. doi: https://doi.org/10.1155/2013/459573.

[9] D. De Battista, S. G. Fabri, M. K. Bugeja, and M. A. Azzopardi. Pocketqube pico-satellite attitude control: Implementation and testing. *IEEE Journal on Miniaturization for Air and Space Systems*, 1(2):90–102, 2020. doi: 10.1109/JMASS.2020.3004410.

[10] European Space Agency. Drama — debris risk assessment and mitigation analysis tool. `https://sdup.esoc.esa.int/discosweb/drama`, 2023. Version 3.1.0.

[11] NASA Goddard Space Flight Center. General mission analysis tool (gmat). `https://gmat.gsfc.nasa.gov`, 2023. Version R2023a.

[12] Andrew T. Harris, Christopher D. Petersen, and Hanspeter Schaub. Linear coupled attitude–orbit control through aerodynamic drag. *Journal of Guidance, Control, and Dynamics*, 43(1):122–131, 2020. doi: 10.2514/1.G004521.

[13] Vishal Ray, Daniel J. Scheeres, and Suood Alnaqbi. Decorrelating density and drag-coefficient through attitude variations. In *Proceedings of the Advanced Maui Optical and Space Surveillance Technologies Conference (AMOS)*, Maui, Hawaiʻi, 2021. AMOS.

[14] Vishal Ray and Daniel J. Scheeres. Drag coefficient model to track variations due to attitude and orbital motion. *Journal of Guidance, Control, and Dynamics*, 43(10):1915–1926, 2020. doi: 10.2514/1.G004854.

[15] Samir A. Rawashdeh. Attitude analysis of small satellites using model-based simulation. *International Journal of Aerospace Engineering*, 2019:Article ID 3020581, 11 pages, 2019. doi: 10.1155/2019/3020581.

[16] John Kennewell. Satellite orbital decay calculations. Technical report, IPS Radio and Space Services, Sydney, 1999. Updated by Rakesh Panwar. Australian Space Weather Agency, Bureau of Meteorology.

[17] Asma Mohammad Nusrat Aman, Roselina Arelhi, and Nafizah Khan. Studying the effects of disturbance torques on a 2u cubesat in low earth orbits. *Journal of Physics: Conference Series*, 1152(1):012024, jan 2019. doi: 10.1088/1742-6596/1152/1/012024.

[18] Xin Wang, Tingling Ren, Ronglan Wang, Bingxian Luo, Ercha Aa, Lei Cai, Ming Li, Juan Miao, Siqing Liu, and Jiancun Gong. Estimates of spherical satellite drag coefficients in the upper thermosphere during different geomagnetic conditions. *Space Weather*, 22(11):e2024SW003974, 2024. doi: https://doi.org/10.1029/2024SW003974.

[19] Abdul Majid, Muhammad Naeem Owais, and Muhammad Nauman Qureshi. Aerodynamic drag computation of lower earth orbit (leo) satellites. *Journal of Space Technology*, 8(1):82–89, July 2018. ISSN: Not specified.

[20] David A. Vallado. *Fundamentals of Astrodynamics and Applications*. Microcosm Press, 2013.

[21] David A Vallado and Paul J Cefola. Two-line element sets–practice and use. In *63rd International Astronautical Congress, Naples, Italy*, pages 1–14, 2012.

[22] Brian Coffee, Rebecca Bishop, and Kerri Cahoy. Propagation of cubesats in leo using norad two line element sets: Accuracy and update frequency. 08 2013. ISBN: 978-1-62410-224-0. doi: 10.2514/6.2013-4944.

[23] David J. Gondelach and Richard Linares. Real-time thermospheric density estimation via two-line element data assimilation. *Space Weather*, 18(2):e2019SW002356, 2020. doi: https://doi.org/10.1029/2019SW002356.